System Simulation of a GLV Projection System

Timothy P. Kurzweg[a], Jose A. Martinez[b], Steven P. Levitan[b*],
Abhijit J. Davare[c], Mark Kahrs[b], Donald M. Chiarulli[d]
[a]Drexel University, ECE Department, Philadelphia, PA USA 19104
[b]University of Pittsburgh, EE Department, Pittsburgh, PA USA 15261
[c]University of California at Berkeley, EECS Department, Berkeley, CA USA 94720
[d]University of Pittsburgh, CS Department, Pittsburgh, PA USA 15260

ABSTRACT

In this paper, we present a system-level simulation and analysis of a diffractive optical MEM Grating Light Valve. The simulations are performed in a system-level multi-domain CAD framework developed at the University of Pittsburgh. Including the electrical, mechanical, and optical domains, this framework allows the user to design micro-optical systems by examining performance measures of the entire system. In this paper, we provide a brief background of the models that are used for signal and device simulation, and use these results for the simulation and analysis of the promising GLV device for applications in a projection system.
Keywords: GLV, system-level modeling, multi-domain simulation

1. INTRODUCTION

The Grating Light Valve (GLV) is one of the more promising optical micro-electrical-mechanical (MEMS) components, having many display applications, including digital projection, HDTV, and vehicle displays [1]. The GLV is a MEM phase grating made from parallel rows of reflective ribbons. When all the ribbons are in the same plane, incident light that strikes normal to the surface reflects 180 degrees off the GLV. However, if alternating ribbons are moved down a quarter of a wavelength ($\lambda/4$), a "square-well" diffraction pattern is created, and the light is reflected at an angle from that of the incident light. The angle of reflection depends on the width of the ribbons and the wavelength of the incident light. Figure 1 shows the ribbons, from both a top and side view, and also the reflection patterns for both positions of the ribbons.

The GLV component is fabricated using standard silicon VLSI technology, with ribbon dimensions approximately 3-5 μm wide and 20-100 μm long [1]. Each ribbon moves through electro-static attraction between the ribbon and an electrode fabricated underneath the ribbon. This electro-static attraction moves the ribbons only a few hundred nanometers, resulting in an approximate switching time of 20 nsec. Since the simulation of a GLV system relies on the optical wavefront, the mechanical displacement of the ribbons, and the electro-static attraction between the ribbons and the substrate, a CAD tool that can model the multi-domains and interactions between these domains is required.

The creation of simulation tools for multi-domain micro-systems (MSMD) systems is challenging because these systems span the physical domains of electronics, photonics, and mechanics, as well as multiple orders of magnitude in both time and length scales. The difficulties are compounded by the fact that computational performance and accuracy are directly
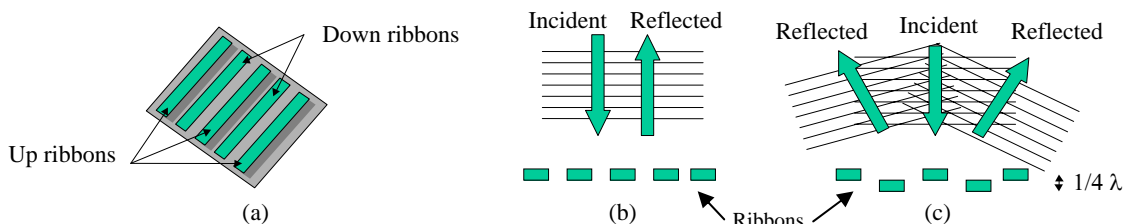
Figure 1: GLV Device (a) Top View and Side View Operation for (b) Up Ribbons and (c) Down Ribbons

* steve@ee.pitt.edu; phone 1 412 648 9663; fax 1 412-624-9663; http://kona.ee.pitt.edu/pittcad

related to the level of detail in the underlying models. Multi-domain micro-systems are currently simulated by point-tools using component level models performed at the physical, or device, level. Device level models focus on explicitly modeling the processes within the physical structure of a device such as electromagnetic fields, fluxes, mechanical stresses, and thermal gradients. These are typically described by partial differential equations in both space and time. Device-based tools are typically domain specific and computationally complex. In contrast, system-level tools are designed to include multiple domains and allow efficient system simulation, by modeling components by their functionality, or behavior, rather than their physical construction. Behavioral level models capture the above mention distributed effects in terms of parameters, and the models focus on the relationships between these parameters and state variables (e.g., optical intensity, phase, current, voltage, displacement, or temperature) as a set of temporal linear or non-linear differential equations in both space and time.

The advantage of having a behavioral representation is that we can simulate electronic, mechanical, and optical models in a single mixed-domain simulation environment. Behavioral models also provide a mechanism for varying the degree of accuracy of the simulation without changing the environment or the models. However, this approach brings the challenge of choosing which behavioral modeling techniques will be best for accurate and fast characterization of the varied components used in multi-domain microsystems.

In the next two sections, we present a review of the models for electrical, mechanical, and optical signals and components found within the GLV simulation. The paper will be concluded with simulations and analysis of a projection system using the GLV device.

2. ELECTRICAL AND MECHANICAL MODELING

For both electrical and mechanical modeling we use a piece-wise linear (PWL) technique described in [2]. In this section, we present some of the details of modeling in both the electrical and mechanical domains.

2.1. Electrical Simulation

For electrical simulations, we first perform linear and non-linear sub-block decomposition of the circuit model of the device. This decomposes the design into a linear multi-port sub-block section and non-linear sub-blocks. The linear multi-port sub-block can be thought of as characterizing the interconnection network and parasitic elements, while the non-linear sub-blocks characterize elements with active non-linear behaviors.

In the second step, a Modified Nodal Analysis (MNA) [3][4] is used to create a mathematical representation for the device. This is shown in Figure 2(a) for electrical components. In this expression [S] is the storage element matrix, [G] is the conductance matrix, [x] is the vector of state variables, [B] is a connectivity matrix, [u] is the excitation vector, and [I] is the current vector [3][4][5].

The linear sub-block elements are directly mapped into this representation, but the non-linear elements need to first undergo a further transformation. We perform piecewise modeling for each non-linear sub-block. This technique, as explained in [2], translates the structure and behavior of these elements into the form of placeholders for their MNA templates. The templates give us the ability to change models for the non-linear devices based on changes in conditions in the circuit, and thus the regions of operation of each element. The templates generated can then be integrated to the general MNA containing the linear components adding their matrix contents to their corresponding counterparts. Once the integrated MNA is formed, a linear analysis can be performed to obtain the solution of the system.

Modified Nodal Matrix representation:

$$[S][x'] = -[G][x] + [B][u]; \qquad [I] = [B^T][x]$$

[S] Storage element matrix
[G] Conductance matrix
[x] State variables
[B] Connectivity matrix
[u] Excitation vector
[I] Current vector.

[S]$_T$ Template from a *bounded* non-linear element (i.e., nodes <N)

(a)

General motion equation

$$F = [K][U] + [B][\dot{U}] + [M][\ddot{U}]$$

Standard ODE Transformation

$$\begin{bmatrix} 0 & M \\ M & B \end{bmatrix}\begin{bmatrix} \ddot{U} \\ \dot{U} \end{bmatrix} + \begin{bmatrix} -M & 0 \\ 0 & K \end{bmatrix}\begin{bmatrix} \dot{U} \\ U \end{bmatrix} = \begin{bmatrix} 0 \\ I \end{bmatrix}F$$

Templates for every basic element (e.g. beam)

$$X = \begin{bmatrix} \dot{U} \\ U \end{bmatrix}; \quad [Mb]\dot{X} + [Mk]X = [E]F$$

(b)

Figure 2: MNA description for (a)Electrical and (b)Mechanical components

The MNA representation is initialized by the application of values for the state variables of the component. For the non-linear elements, the definitions of the regions of operation are compared against these state variables, and the MNA representation is updated accordingly. This MNA representation is then passed to the solver, which returns the new set of state variables.

During each time step in the simulation, the state variables in the module will change and might cause the non-linear elements to change regions of operation. Therefore, we re-compute the solution caused by changes between piecewise models. In general, depending on the number of regions of operation used in the piecewise linear model, there are a large number of time steps during which the system representation is unchanged, justifying the computational savings of this technique.

Understanding that the degree of accuracy of piecewise linear models depends strongly on the step size chosen for the time base, an adaptive control method is used [5]. The inclusion of the samples during fast transitions or suppression of samples during "steady state" periods optimizes the number of events used in the simulation.

For electrical components, the inputs and outputs of the component are identified nodes of the network. The output nodes have characteristic output impedances, providing impedance matching between electrical components. This impedance, together with a piecewise linear voltage waveform is passed to other components by the discrete event simulation engine at the system level.

While we have used electronic components for the preceding discussion, these same techniques apply to other domains. For mechanical components, we can derive a similar template based structure for composition into a MNA formulation as explained next. This is described in the next section.

2.2. Mechanical Behavioral Modeling

The model for a mechanical device can be summarized as a set of differential equations that define its dynamics as a reaction to external forces. With damping forces proportional to the velocity, the equation of motion for a mechanical structure with viscous damping effects is: $F = KU + BU' + MU''$ [6], where, K is the stiffness matrix, U is the displacement vector, B is the damping matrix, U' is the velocity vector, M is the mass matrix, U'' is the acceleration vector, and F is the vector of external forces affecting the structure. Similar to the previous case, this equation represents a set of linear ODEs if the characteristic matrices K, B, and M are static and independent of the dynamics in the body. If the matrixes are not static and independent (e.g., the case of aerodynamic load effects), they represent a set of non-linear ODEs.

Using a modification of Duncan's reduction technique for vibration analysis in damped structural systems [7], we reduce the above general mechanical motion equation to a standard first order form. This gives a complete characterization of a mechanical system, as shown in Figure 2(b). Each mechanical element (beam, plate, etc.) is characterized by a template consisting of the set of matrices Mb and Mk, composed of matrices B, M, and K. If the dimensional displacements are constrained to be small and the shear deformations are ignored, the derivation of Mb and Mk is simplified and independent of the state variables in the system. Typically, this element is only a part of a bigger device made from individual components that are characterized using similar expressions. The generalization of the previous case to an assembly of elements or mechanical structures is fairly straightforward [5][6].

We use dynamic control of the sampling rate in the mechanical domain based on the Nyquist criteria of the highest significant modal frequency for the structure. The allowed sampling rate is lower than half of the period of the highest modal frequency. This allows us to optimize the samples used in this domain while still completely characterizing its dynamic behavior. There can be several orders of magnitude reduction in the sampling rate compared to the electrical domain because of the difference in dynamics.

For the electrostatic modeling of forces over the mechanical structure, we consider a single elemental beam, as shown in Figure 3. The surface defined by this single flat basic element intercepts the substrate plane in a line that can be considered a virtual axis for the relative coordinate system. This element is considered a part of a "structural ensemble" which makes up a complete beam. The modeling is based on considering the sub-structure as an inclined flat capacitor.
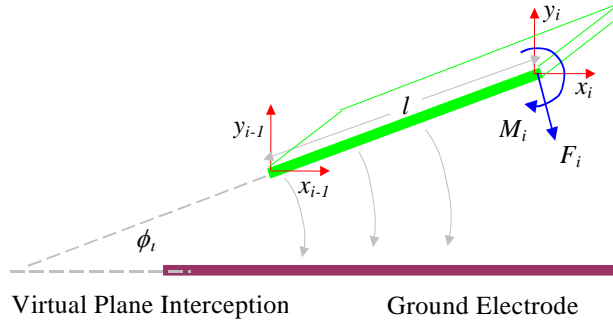
Figure 3: Electrostatic modeling on a single elemental beam

The distributed electrostatic forces are analytically represented as concentrated forces applied over the last node of the basic beam. The electrostatic force over the element i is given by:

$$F_i = \left(\frac{\varepsilon w V^2}{l} \right) \frac{(y_i - y_{i-1})^2}{\phi_i^2 y_i y_{i-1}}$$

In this expression, the ϕ represents the inclined angle between both planes, V is the applied voltage, l is the length of the elemental beam, w is the width of that element, y_i and y_{i-1} are the y coordinates of the nodes in the global reference system, and ε is the electric permitivity of the medium between the plates.

The electrostatic torque over the element i is given by:

$$M_i = F_i \frac{\Delta x_i}{l} x_{i-1} + F_i \frac{\Delta x_i}{l} \frac{\Delta x_i}{\Delta y_i} y_{i-1} \left(\frac{y_i}{\Delta y_i} \ln\left(\frac{y_i}{y_{i-1}} \right) - 1 \right) + F_i \frac{y_i}{l} y_{i-1} \ln\left(\frac{y_i}{y_{i-1}} \right)$$

These analytical expressions describe the electro-static behavior for the basic element. Using a PWL linearization technique as the one previously described, these expressions are reduced to linear templates that capture their non-linear behavior through a set of regions of operations. These models can then be integrated to the representation of the structural ensemble.

As can be seen, for this model there is no distinction between variables from either the mechanical or the electrical domains. The direct relationship between the domains is the key for this multi-domain model. In fact, it is these relationships that embody the behavior of the electrostatic transducer and govern the conversion of energy between domains.

The use of a PWL general solver for mechanical simulation decreases the computational task and allows for a trade-off between accuracy and speed. The additional advantage of using the same technique to characterize electrical and mechanical models allows us to easily merge both technologies in complex devices that interact in mixed domains. However, for the optical domain, we need to explicitly consider the propagation medium as well as the optical components themselves. This is because in free-space optical signals do not simply propagate point-to-point.

3. OPTICAL PROPAGATION

When optical wavefronts interact with the small feature sizes of micro-systems, many of the common optical propagation modeling techniques become invalid, and full vector or scalar solutions to Maxwell's equations are required for accurate simulation [8]. However, these accurate solutions are computationally intensive, making interactive design between system designer and CAD tool almost impossible. As more optical components are introduced into micro-systems and the systems become more complex, the demand for computationally efficient simulation tools increases.
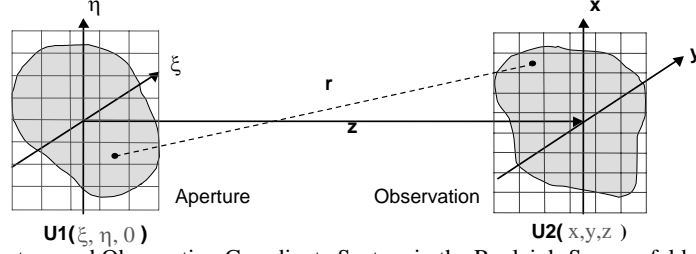
Figure 4: Aperture and Observation Coordinate System in the Rayleigh-Sommerfeld Approximation

Therefore, the problem of optical modeling in MSMD microsystems is two-fold: first, a rigorous model is needed to model optical propagation, and, second, the model must be computationally efficient.

To reduce the computational resources of modeling the optical wavefront completely by the vector solution of Maxwell's equations, a scalar representation is commonly used. Scalar optics are defined by summarizing the electric field vector, $\vec{E}$, and the magnetic field vector, $\vec{H}$, by a single complex scalar, U. This replacement is valid if the propagation medium is dielectric, isotropic, homogenous, nondispersive, and nonmagnetic. Propagation through free-space meets these requirements.

This complex scalar must satisfy the Helmholtz wave equation, $(\nabla^2 + k^2)U = 0$, where, the wave number, $k = 2\pi/\lambda$. With use of Green's theorem, the Rayleigh-Sommerfeld formulation is derived from the wave equation for the propagation of light in free-space from the aperture plane $(\xi, \eta, 0)$ to a parallel observation plane (x, y, z), as seen in Figure 4 [9]:

$$U(x, y, z) = \frac{z}{j\lambda} \iint_\Sigma U(\xi, \eta, 0) \frac{\exp(jkr)}{r^2} \, \partial\xi \partial\eta$$

where, $r = \sqrt{z^2 + (x - \xi)^2 + (y - \eta)^2}$, Σ is the area of the aperture, and z is the distance that the light is propagated from an aperture plane $(z = 0)$ to the observation plane. The formulation is valid as long as both the propagation distance and the aperture size are greater than the wavelength of light. These restrictions are based on the boundary conditions of the Rayleigh-Sommerfeld formulation, and the fact that the electric and magnetic fields cannot be treated independently at the boundaries of the aperture [9]. To compute the complex wavefront at the observation plane, each plane is discretized into an NxN mesh. Using a direct integration technique, the computational order of the Rayleigh-Sommerfeld formulation is $O(N^4)$.

The far (Fraunhofer) and near (Fresnel) field approximations of the scalar formulation reduce the computational demand, using a FFT for optical propagation. However, we have shown that these techniques are not valid for typical micro-system dimensions [8]. In the interest of reducing the computational load of using a full scalar technique, we have recast the Rayleigh-Sommerfeld formulation using an angular spectrum technique.

3.1. Angular Spectrum Technique

As an alternative to direct integration over the surface of the wavefront, the Rayleigh-Sommerfeld formulation can also be solved using a technique that is similar to solving linear, space invariant systems. Re-examining the Rayleigh-Sommerfeld formulation, it can be seen that the equation is in the form of a convolution between the complex wavefront and the propagation through free space [10]. The Fourier transform of the complex optical wavefront results in a set of plane waves traveling in different directions away from the surface [9]. Each plane wave is identified by the components of the angular spectrum. At the observation plane, the plane waves are summed together by performing an inverse Fourier transform, resulting in the propagated complex optical wavefront at the observation plane. Brief details of the technique follow.

To solve the Rayleigh-Sommerfeld formulation with the angular spectrum technique, we first examine the complex wavefront at the aperture plane. The wave function $U(x,y,z)$ has a 2D Fourier transform, $A(v_x,v_y,0)$, in terms of angular frequencies, v_x and v_y.

$$A(v_x,v_y,0) = \iint U(x,y,0)\exp[-j2\pi(v_x x + v_y y)]\,\partial x \partial y, \text{ where, } v_x = \sin\theta_x / \lambda \text{ and } v_y = \sin\theta_y / \lambda.$$

From the equation, the plane waves are defined by $\exp[-j2\pi(v_x x + v_y y)]$ and the spatial frequencies define the directional cosines, $\sin(\theta_x)$ and $\sin(\theta_y)$, of the plane waves propagating from the origin of the aperture plane's coordinate system.

The free-space transfer function in the frequency domain has been computed by satisfying the Helmhotz equation with the propagated complex wave function, $U(x,y,z)$:

$$A(v_x,v_y,z) = A(v_x,v_y,0)\exp\left\{ jz2\pi\sqrt{\frac{1}{\lambda^2} - v_x^2 - v_y^2} \right\}$$

This describes the phase difference that each of the plane waves, differentiated by the spatial frequencies, experiences due to the propagation between the parallel planes. Therefore, the wave function after propagation can be transformed back into the spatial domain with the following inverse Fourier transform:

$$U(x,y,z) = \iint A(v_x,v_y,0)\exp\left\{ jz2\pi\sqrt{\frac{1}{\lambda^2} - v_x^2 - v_y^2} \right\}\exp[j2\pi(v_x x + v_y y)]\,\partial v_x \partial v_y$$

The advantage of using the angular spectrum to model light propagation is that the method is based on the Fourier transform. The computational order of the FFT for a 2D input is $O(N^2 log_2 N)$.

In continuous theory, the angular spectrum method is an exact solution of the Rayleigh-Sommerfeld formulation. However, when using a discrete Fourier transform the accuracy of the angular spectrum method depends on the resolution of the aperture and observation plane mesh. We have determined in 2D space that with a mesh spacing of Δx, $\Delta y < \lambda/2$, the angular spectrum decomposition will ensure plane waves propagating from aperture to observation plane in a complete half circle, that is, between -90 and $+90$ degrees [11]. For many simulation systems without large degrees of tilt and hard diffractive apertures, the resolution can be coarser. In systems with high tilts, the resolution is most sensitive.

4. GRATING LIGHT VALVE SIMULATION

In this section, we present simulation and analysis of the GLV system. For the simulations of the GLV, we examine one optical pixel. A projected pixel is diffracted from a GLV composed of 4 ribbons, two stationary and two that are movable [1]. In our simulations, each ribbon has a length of 60 µm, a width of 5 µm, and a thickness of 1.5 µm, for a total GLV pixel size of 60x20 µm. The ribbons are made of silicon nitrite (density 3290 Kg/m^3, Young's modulus 290x10^9 N/m^2), and coated with aluminum for smoothness and reflectivity.

The model of the GLV is two fold: an electro-mechanical model simulating the movement of the ribbons towards the substrate, and the optical model, simulating the reflection of the optical wavefront off of the ribbons. The ribbon is modeled as a thin beam anchored on each end. The beam is modeled as PWL segments, and is electro-statically attracted to the silicon substrate, which is covered with 500 nm of silicon dioxide. The voltage is applied between the ribbon and substrate electrode by a 2-stage CMOS amplifier seen in Figure 5(a). This electrical driver is modeled as described previously, and its response to a 0-5(V) input ramp is also shown in Figure 5(b). The air gap between the ribbons and the surface is 0.65 µm. The effect of the ribbon movement is optically modeled as a phase grating, where the light that strikes the down ribbons propagates further than the light that strikes the up ribbons. In our model, light reflecting from the down ribbons is multiplied by a phase term. The phase term is similar to a propagation term through
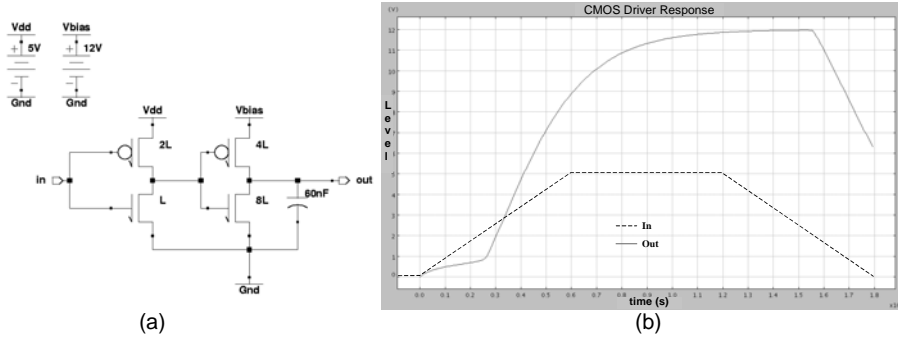
Figure 5: 2 Stage CMOS Driver used as the GLV Input (a) and Response to Ramped Input (b)

a medium: $U_{down\_ribbon}=Uexp(j2kd)$, where, d is the distance that the ribbon is moved towards the substrate and k is the wave number, $k=2\pi/\lambda$.

Since the ribbon ends are anchored, the alternating ribbons are not flat as they are electro-statically attracted to the substrate. As expected the beams are curved. In the simulations, the ribbon is composed of an equal sized number, N, of segments or basic beams, totaling $N+1$ nodes. The layered shape of the ribbon with forces and movement limited to one plane justify the use of the basic beam element for the modeling of the mechanical structure. The analysis is reduced to a two-dimensional problem in the plane of the displacement. The accuracy of the mechanical simulation can be increased if a larger number of these basic elements are used at the cost of an increase in computation time. The resolution of higher fundamental nodal frequencies is proportional to the number of these segments. Simulation output data show the shape of the curved beams as the voltage between the ribbons and the substrate electrode is varied between 0 and 12 (V). This linear ramp is completed in 600 μs. For these simulations, we examine cases with 5, 11, 21, and 41 nodes. The mechanical deformation of the ribbon for the 11 and 41 node case is displayed in Figure 6(a) and (b). Note that the y-axis is in nanometers and the x-axis is in microns.

We first perform simulations in which ideal alternating flat non-anchored ribbons move toward the substrate. We assume an incident plane wave of green light (λ = 520 nm) striking the grating, with the square-well diffraction period defined by the ribbon width. We simulate the GLV in both cases, that is, when all the ribbons are on the same plane and when the alternating ribbons are moved downward a distance of 130 nm, or λ/4. In this example, the light is reflected off of the grating and propagated 1000 μm to an observation plane. An optical window of 400x400 μm is used, with an optical meshing equal to 256x256. Intensity contours of the optical waveform at the observation plane are presented in Figure 7(a) for the case when the ribbons are all aligned, and when alternating ribbons are pulled down a distance equal to a quarter of the wavelength of the incident light, Figure 7(b). Notice that the output optical waveform's height and widths are not equal. This is due to the rectangular shape of the GLV pixel, 60x20 μm. Also notice that the optical waveform appears to be in two lobes. This is a near-field optical effect of light propagating through a rectangular aperture and demonstrates that in this system, light propagating 1000 μm is not in the far-field. This near-field effect highlights that the common scalar approximations, such as the Fraunhofer far-field approximation, would provide inaccurate simulation results, and the full Rayleigh-Sommerfeld formulation is required for accurate results.

The example is now re-simulated with more realistic curved ribbons. When curved ribbons are attracted down towards
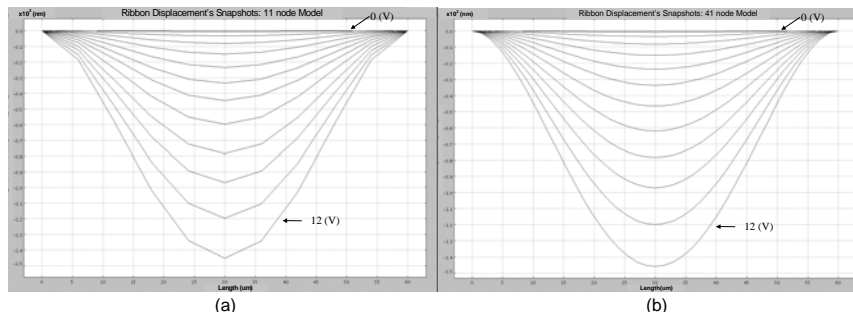
Figure 6: Ribbon Displacement at 1(V) increment (a) 11 node Model (b) 41 node Model
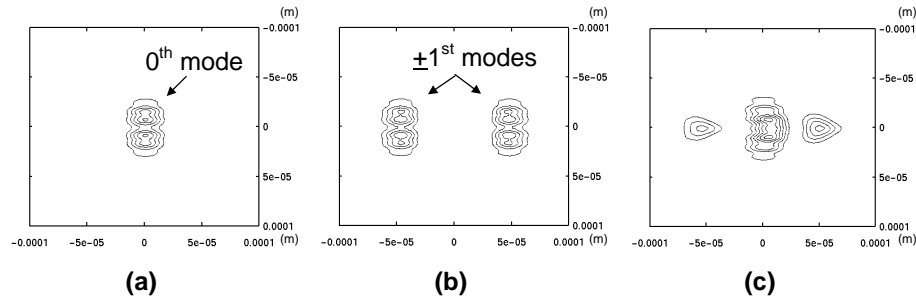
Figure 7: GLV Operation (a) Ribbons all up (b) Ideal Ribbon Displacement (c) Curved Ribbon Displacement

the substrate, the diffractive optical output is no longer ideal, as can be seen in the intensity contour of Fig. 7(c). Since the beam is curved from the anchors, an ideal square well diffraction pattern is no longer achieved, and the optical intensity contour appears to be a mix of the ideal cases seen in Figure 7(a) and (b). The light reflecting from the middle of the ribbon, which is pulled down approximately $\lambda/4$ (130 nm), creates the $\pm$1st diffractive modes. These modes are now more circular, since effectively a 20x20 μm square well is created in the center of the GLV device. The remainder of the light reflecting off the ribbons reflects straight off the GLV and creates the light found in the 0th mode.

In the next simulation, we performed a transient sweep of the applied voltage between the ribbon and the substrate electrode, from 0 to 12 V, with a complete switch occurring in 600 μs. The rest of the system setup is exactly the same as before. However, this time, we simulate the encircled power captured in the +1st diffraction mode for different ribbon depths. To simulate this, a circular detector (radius=10μm) is placed on the +1st mode.

Figure 8 shows two graphs. The first shows the displacement of the center ribbon node and the input voltage with respect to time. From this result, we present the second graph in which we show how the ribbon movement affects the (normalized) encircled energy captured on the first mode detector. We can see, as the ribbons are attracted to the substrate, more optical power is diffracted into the non-zero modes. As the ribbons reach the $\lambda/4$ point (130 nm), the diffractive power peaks in the +1st mode. Beneath the two graphs in the figure are intensity contours of selected wavefronts during the transient simulation, along with markings of the system origin and circular detector position. From these wavefronts, interesting diffractive effects can be observed. As expected, when there is little voltage applied, all the light is in the 0th mode. As the ribbons move downward about $\lambda/8$ (65 nm), the energy in the $\pm$1st modes is clearly defined. As the gratings move closer to the $\lambda/4$ point, more power is shifted from the 0th mode into the $\pm$1st modes. As the ribbons start to return to their original position, the optical power shifts back into the 0th mode.

To show system-level multi-domain modeling and the ability to trade-off different technologies, we next examine realistic gaps between the GLV ribbons. The gap between the ribbons depends on the feature size of the lithographic tools used to fabricate the MEMS device [14]. In this simulation, we use the same anchored GLV ribbons and electrical drivers as simulated previsouly, however, a gap between the adjacent ribbons is now modeled. In these simulations, we model the gaps between the GLV ribbons to be completely absorbing. In Figure 9, we present intensity cross-sections of a plane wave striking the entire GLV with alternating ribbons attracted to the substrate with 12 V and propagating 1000 μm. Simulations are performed with GLV ribbon gaps of 0, 0.5, 1, and 2 μm. As expected, the ribbon gaps each produce a different diffractive phase front, resulting in a different diffractive angle of the odd modes. The diffraction
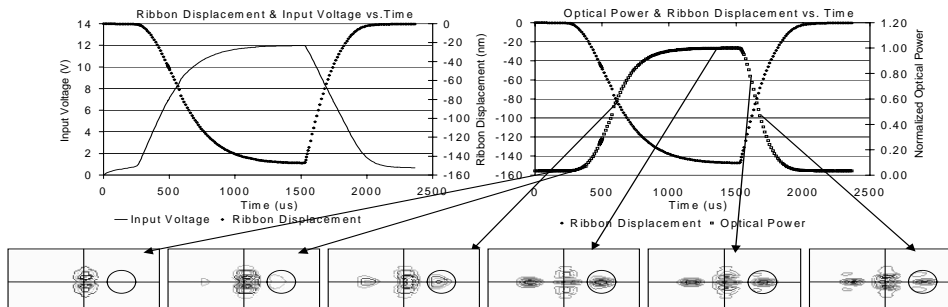
Figure 8: GLV Simulation Graphs and Intensity Contours
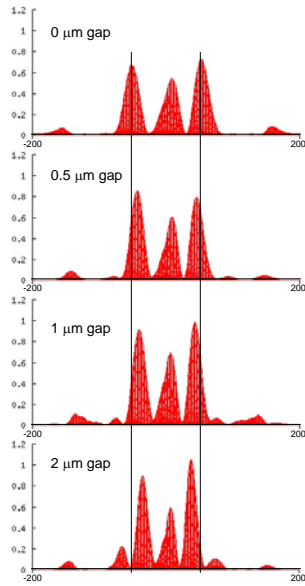
Figure 9: Intensity Cross-sections for GLV Gaps of 0,0.5,1,2 μm
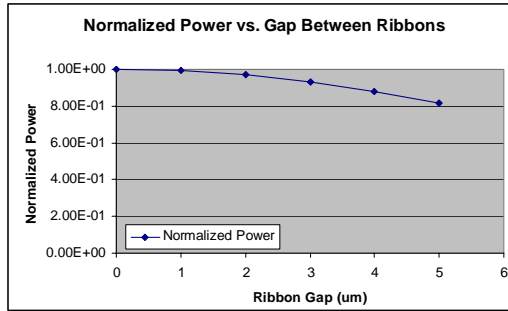
Figure 10: Gap between ribbons vs. Power capture on 1st diffractive mode

angle can be seen to get smaller as the gap between the ribbons gets larger. To illustrate this, a line is drawn in Figure 9 relating the position of the $\pm1^{st}$ modes in the case when using a GLV with no gaps and the other three cases of using a GLV with gaps between the ribbons. Additionally, it can be seen that the optical interference of light diffracting off of the gaped diffractive pattern alters the peak intensity and width of the odd modes.

Illuminating the GLV with a finite dimensioned plane wave, we can evaluate the ribbon gaps in terms of insertion loss. In these simulations, we use an input plane wave, with a size limited to 20x20 μm. As in previous simulations, the GLV is composed of 4 ribbons, with a total area of 60x20 μm. With this input source, only the middle of the ribbons are being illuminated, resulting in an ideal diffraction square well, with the light diffracting only in the odd modes. We now evaluate the power captured in the positive first diffractive mode and how it is affected by the ribbon gaps. To evaluate the optical power in the 1st mode, the plane wave is diffracted off of the GLV ribbons (excited by a 12 V input), propagated 1000 μm, and detected on a circular detector (radius=10μm) placed on the $+1^{st}$ mode. In Figure 10, a graph comparing received normalized power and the gap size is shown for gaps of 0, 1, 2, 3, 4, and 5 μm. As can be seen, with a gap size of less than 3 μm, an optical efficiency over 90% can be achieved. Using a simulation tool like ours, the system designer can design the system taking into account the fabrication technology, in this case, the feature size used to create the GLV.

In the next simulation, we present a full system-level example as we expand the system to show a complete end-to-end link used in a configuration of a color projection system. The system is shown in Figure 11(a). In this system, we model light, passing through a color wheel, striking a prism, reflecting off the GLV device, past a screen, focused by a lens, and striking a detector [1]. In this system, when the GLV ribbons are all up, the screen blocks the light's 0th mode and the pixel is "off". When the alternating ribbons are pulled down, the lens focuses the light found in the $\pm1^{st}$ modes and converges them to the center of the system, forming the "on" pixel. In this case, when the pixel is on, the screen blocks the light that is found in the 0th mode, as seen previously in Figure 7(c). Using a spinning color wheel to change the wavelength of the incident light, a frame-sequential GLV projection system uses red (680 nm), green (520 nm), and blue
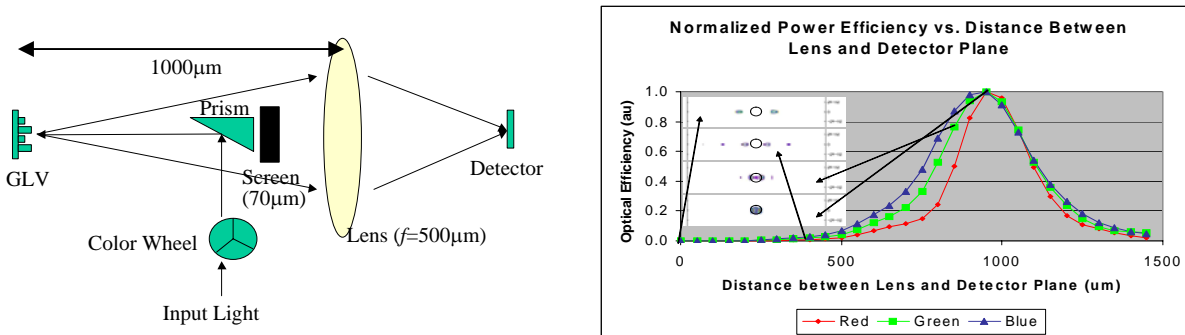
Figure 11: (a) End-to-End System Link (b) Wavelength Detected Power vs. Wavelength

(470 nm) light on the same grating [1]. Since the same grating is used for all wavelengths of light, the grating movement is tuned for the middle frequency: approximately, 130 nm ($\lambda_{green}/4$).

We analyze the system by looking at the amount of optical power that is being received on a centered circular detector (radius 10μm) for the each of the different wavelengths of light when the pixel is "on", that is, the mechanical ribbons are pulled down λ/4. The detector position is swept a through a range of 0 to 1450 μm past the focusing lens ($f = 500$ μm). For each wavelength, the graph in Figure 11(b) shows the normalized power received on the circular detector at the defined distance past the lens.   Selected intensity contours of the green wavefront along the transient swept are included in Figure 11(b). For clarity, the detector's size and position is superimposed onto the intensity contours. As can be seen in the graph, for distances between the lens and the detector less than 600 μm, the light remains in its positive and negative 1st modes, as the convergence of the beams has not occurred, resulting in zero power being received on the center detector. As expected, each of the wavelengths focuses at a different rate, as shown by each the wavelength's specific curve in Figure 11(b). However, it can also be seen that all wavelengths focus and achieve detected maximum power at a distance past the lens of approximately 950 μm, or roughly twice the lens' focal length. At this point, all three colors project on top of each other, creating a color pixel in the focal plane. With additional optics, this focal plane can be projected to a screen outside the projector. This simulation has shown that the GLV grating, although tuned for the green wavelength, can be used for all three wavelengths.

4.1.   System-Level Simulation Performance

Using the same simulation environment we conducted the following tests to illustrate the speed/fidelity tradeoffs that can be done with a system level simulation tool.

The accuracy of the mechanical simulation was compared to modal analysis of the ribbon using ANSYS [12]. An 11-node model matches the nine first modal frequencies with a maximum difference of 2.24 % at the highest frequency. For a 21-node model the 10th modal frequency differs by less than 0.59 %. A 41-node model reduces this difference to 0.15%. As expected, to accurately capture higher modal frequencies, a larger discretization is required. Similar performance in the mechanical simulation of MEMS using this technique and its verification against NODAS [13] and ANSYS has previously been reported [2][5].

Figure 12 shows the dynamic response of the ribbon driven at a high switching frequency. The high stiffness of the structure gives it a fast response time as observed. However, under this stimulus, resonant effects are observed in the displacement of the nodes. The visible pattern of damped oscillations shows that the stiffness affects maximum operating speed of this device. The damping of MEM structures under laminar fluid is a difficult problem. In ANSYS, the damping is characterized as ideal spring damping elements to avoid the costly computation of a complete fluid analysis using Stoke's formulation. The dynamic response of the ribbon driven at a high frequency in ANSYS is shown in Figure 12(a). In our methodology, we chose to include the effect directly in the damping matrix of the structure, which allows the damping to affect displacement in every degree of freedom of the element. Our result is shown in Figure 12(b). However, we are still using a typical constant value for this effect. A more rigorous damping analysis considering the non-linear laminar fluidic effect over the structure is required for both techniques and it is currently under development in our tool.

(a)   (b)
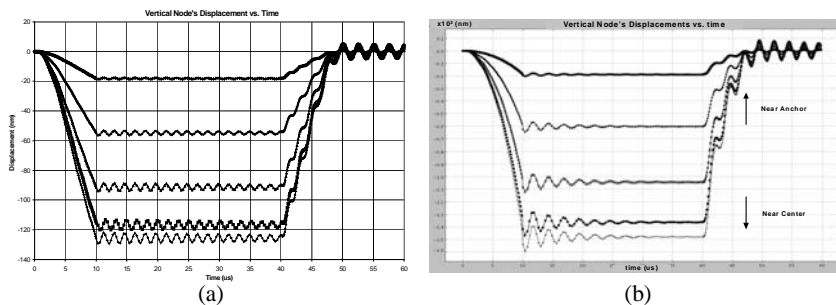
Φιγυρε 12: Νοδαλ δισπλαχεμεντσ ιν 11−νοδε ριββον μοδελ ωιτη ηιγη φρεθυενχψ δριϖε σιγναλ (10 μs switching time)
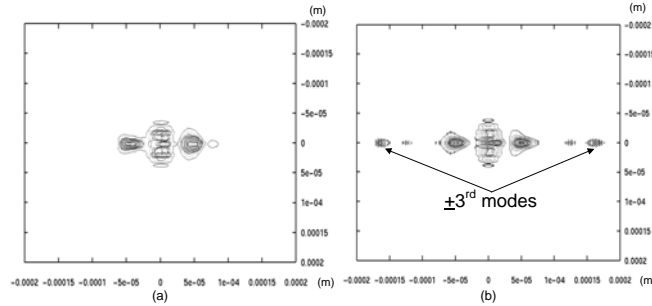
Figure 13: Diffraction pattern at maximum ribbon displacement, (a) Ribbon model with 5 segments and 128x128 mesh for optical wavefront (b) Ribbon model with 41 segments and 512x512 mesh for optical wavefront.

Figure 13(a) shows the diffraction pattern at maximum ribbon displacement for a ribbon modeled with 5 segments and the scalar wavefront modeled with a 128x128 mesh. Figure 13(b) shows the same system modeled with a 41 segment ribbon and a 512x512 mesh. What can be seen is the improvement in the degree of resolution of the wavefront, in particular the appearance of low power 3rd order modes.

Table 1 shows system simulation time as a function of both the scalar mesh resolution and the number of segments in the ribbon. For the simulations, a dual Pentium 1.7 GHz/Xeon processor with 4 GB RAM/PC800, running under Red Hat Linux 7.1.was used. The mechanical subsystem time includes the initialization of the MNA as well as the solution times for the entire movement for the 2.4 ms stimulus. The optical subsystem time includes both the scalar propagation time and the detector power integration time. The optical propagation time averaged 30 ms for the 128x128 case and 490 ms for the 512x512 case, while the integration time went from 2 seconds to 41 seconds respectively. We note that for typical systems, optical detection need only be done at the receivers after several stages of optical propagation. The system time included the electrical simulation of the CMOS driver, as well as initialization overhead. In previous work, we reported that the PWL electrical simulator was able to simulate simple CMOS circuits with a relative accuracy of 5% when compared to SPICE and with speedup factors of up to 100 [5].

Table 1: Grating Light Valve System Simulation Time

Segments	128x128			512x512		
	Mechanical	Optical	System	Mechanical	Optical	System
5	0.14	1.99	3.33	0.16	40.79	42.37
11	2.02	2.02	5.30	2.02	41.01	44.49
21	15.60	1.98	19.19	15.43	40.78	58.19
41	119.94	1.99	128.81	124.40	40.33	167.68

What is interesting to note in this discussion and in Figures 12 and 13, is the range of simulation time: 3 seconds for the 5-element, 128x128 case to 168 seconds for the 41-element, 512x512 case and the commensurate increase in fidelity of the resulting optical waveforms and mechanical characterizations achieved. This illustrates that we can use the same behavioral descriptions, in the same system-level simulation environment, to perform both interactive "what if" design exploration as well as more detailed investigations of higher order effects by simply changing the simulation parameters (e.g., optical mesh size, number of mechanical nodes, number of regions of operation for non-linear elements, and minimum timestep) without recourse to lower level simulation tools.

5. SUMMARY AND CONCLUSIONS

In this paper, we have shown simulations of the GLV device with applications toward projection systems. In this work, we have addressed the need for a consistent behavioral modeling methodology that spans the multiple technologies of electronics, mechanics, and optics. We have also shown how to use piecewise linear models to capture the behavior of non-linear elements in these domains. Our simulation method at the component level, based on Modified Nodal Analysis, allows the designer to trade modeling and simulation accuracy for simulation speed. Our angular spectrum scalar representation for free-space optical signal propagation allows us to model micro-optical components in the near-

field and still perform system level simulations in reasonable time, supporting the system designer in performing design trade-offs in an interactive design environment. With a tool like this, a complete system analysis of a multi-domain system, like the GLV, can be simulated in a single environment.

REFERENCES

[1] D. M. Bloom, "The Grating Light Valve: Revolutionizing Display Technology," in *Proc. of Photonics West*, Projection Displays III, 1997.

[2] S. P. Levitan, J. A. Martinez, T. P. Kurzweg, A. J. Davare, M. Kahrs, M. Bails, D. M. Chiarulli, "System Simulation of Mixed-Signal Multi-Domain Microsystems with Piecewise Linear Models," to be published in IEEE Transactions on CAD of Integrated Circuits and Systems, February, 2003.

[3] J. A. Martinez, "Piecewise Linear Simulation of Optoelectronic Devices with Application to MEMS," M.S. Thesis, University of Pittsburgh, Department of Electrical Engineering, 2000.

[4] P. Feldmann, and R. W. Freund, "Efficient linear circuit analysis by Padé approximation via the Lanczos process," *IEEE Trans. Computer-Aided Design*, vol. 14, May. 1995, pp. 639-649.

[5] J. A. Martinez, T. P. Kurzweg, S. P. Levitan, P. J. Marchand, and D. M. Chiarulli, "Mixed-Technology System-Level Simulation", *Analog Integrated Circuits and Signal Processing*, Vol. 29, pp. 127-149, October/November 2001.

[6] J. S. Przemieniecki, *Theory of Matrix Structural Analysis*, McGraw-Hill, New York, New York, 1968.

[7] W. J. Duncan, *Reciprocation of Triply Partitioned Matrices*, J. Roy. Aeron. Soc., vol. 60, 1956, pp. 131-132.

[8] T. P. Kurzweg, S. P. Levitan, J. A. Martinez, P. J. Marchand, and D. M. Chiarulli, "Diffractive Optical Propagation Techniques for a Mixed-Signal CAD Tool," in *Proc. of Optics in Computing (OC2000)*, Quebec City, CA, June 18-23, 2000.

[9] J. W. Goodman, *Introduction to Fourier Optics*, Second Edition (The McGraw-Hill Companies, Inc., 1996).

[10] N. Delen, and B. Hooker, "Free-space Beam Propagation Between Arbitrarily Oriented Planes Based on Full Diffraction Theory: a Fast Fourier Transform Approach," *JOSA*, Vol. 15, No. 4, April 1998, pp. 857-867.

[11] T. P. Kurzweg, "Optical Propagation Methods for System-Level Modeling of Optical MEMS," Ph.D. Thesis, University of Pittsburgh, Department of Electrical Engineering, 2002.

[12] ANSYS, Incorporated, http://www.ansys.com

[13] J. E. Vandemeer, "Nodal Design of Actuators and Sensors (NODAS)," M.S. Thesis, Department of Electrical and Computer Engineering, Carniege Mellon University, Pittsburgh, PA, 1997.

[14] D.T. Amm, R.W. Corrigan, "Optical Performance of the Grating Light Valve Technology," Photonics West-Electronic Imaging, Projection Displays V, 1999.